Bimetallic metal-organic frameworks for efficient visible-light-driven photocatalytic CO_2 reduction and H_2 generation

Chizoba I. Ezugwu [a,*], Srabanti Ghosh [b,c,*], Susmita Bera [b], Marisol Faraldos [d], Marta E.G. Mosquera [e], Roberto Rosal [a]

[a] Department of Analytical Chemistry, Physical Chemistry, and Chemical Engineering, University of Alcala, E-28871 Madrid, Spain
[b] Energy Materials & Devices Division, CSIR - Central Glass and Ceramic Research Institute, 196, Raja S. C. Mullick Road, Kolkata 700032, India
[c] Academy of Scientific & Innovative Research (AcSIR), Ghaziabad, India
[d] Instituto de Catálisis y Petroleoquímica, ICP-CSIC, Marie Curie 2, 28049 Madrid, Spain
[e] Department of Organic and Inorganic Chemistry, Institute of Chemical Research "Andrés M. del Río" (IQAR), University of Alcala, 28805 Alcalá de Henares, Madrid, Spain

A B S T R A C T

A series of robust octahedral bimetallic metal-organic frameworks, NH_2-UiO-66(Zr/M), denoted as Zr/M-ATA, (where M is Fe, Co, or Cu) were prepared by solvothermal de novo reaction of 2-aminoterephthalic acid (denoted as H_2ATA) and mixed metal salts using benzoic acid as a modulator. Photocatalytic studies revealed that Zr/Fe-ATA, Zr/Cu-ATA and Zr/Co-ATA containing double metals outperformed that of the monometallic Zr-ATA. Zr/Cu-ATA displayed excellent performance for visible-light-driven CO_2 reduction with a formate formation rate of 122 µmol h^{-1} $mmol_{MOF}^{-1}$, which is among the highest performance of NH_2-UiO-66 based MOFs. Furthermore, Zr/Cu-ATA is an efficient catalyst that can generate 12.8 mmol of H_2 in 2 h under visible light irradiation. The light absorption band of Zr/Cu-ATA shifted to the near-IR region and the presence of Cu-oxo clusters significantly narrowed the bandgap from 2.95 eV (Zr-ATA) to 1.93 eV (Zr/Cu-ATA). Other photo-electrochemical studies further confirmed that the high catalytic performance of Zr/Cu-ATA can be ascribed to optimized bandgap, facile charge transfer and availability of large number of active sites.

1. Introduction

Continuous CO_2 emission remains the major environmental challenge in this century because its excess in the atmosphere traps heat on earth, resulting in global warming [1]. To address this environmental issue, efficient carbon capture and conversion techniques are highly desirable. Artificial photosynthesis is an emerging technique for using solar energy for the photochemical transformation of carbon dioxide and water into fuels and high value-added chemicals [2]. It is an innovative technology that could simultaneously solve this challenging universal problem of global warming and energy crisis [3,4]. In addition, the H_2 produced from photocatalytic water splitting process can provide a clean and abundant energy source [5,6]. Although, photocatalysts with improved product selectivity have been synthesized, like metal oxides and sulfides (TiO_2, ZnS, and CdS), but persisting issues affecting these materials includes structural tunability, large band gap and fast charge recombination [7–9]. Metal-organic frameworks (MOFs) constitute a family of emerging materials that include photocatalysts with large specific surface area, abundant accessible active sites, easy tunable structure, and modifiable pore environment [10]. The use of electron-rich aromatic polycarboxylate linker as antenna to absorb light, results in charge separation and migration from the linker to the metal cluster, which behaves as quantum dots [11]. Their band gap and the energy position of their band edges can be precisely controlled, making them optimal candidates for CO_2 and H_2O photoreduction [12,13]. Moreover, their catalytic performance can be engineered by enhancing light absorption, conductivity and charge transfer efficiency [14,15].

Bandgap engineering can be achieved by modulating the concentration of amine functionalities in the linker. Hendon et al. analyzed the electronic structure of aminated frameworks and further explored the rule of amine groups in lowering the bandgap of $MIL-125-NH_2$ by increasing the lowest unoccupied molecular orbital (LUMO) without affecting the highest occupied molecular orbital (HOMO) energy level [16]. Since these energy levels, HOMO and LUMO, are mainly

contributed by the linker and the metal clusters, respectively, the strategic modification of these components can be used to achieve the required bandgap [17,18]. Metal node engineering, such as bimetallic MOFs, is a promising strategy for tuning the framework's electronic behaviour. The incorporation of bimetallic nodes creates synergistic effects between different metals, thereby enhancing their intrinsic properties [19]. In essence, bimetallic systems proved to be effective, even the catalytic performance of bimetallic nanoparticle outperformed their monometallic counterpart [20,21]. For example, the efficiency of hydrogen generation of bimetallic Au/Pd supported on reduced graphene oxide performed better than their analogous monometallic sample [22]. Therefore, rational design of bimetallic MOFs may lead to materials with enhanced electronic, optical, and magnetic properties. Since Zr-based MOF photocatalysts are recently gaining attention because of their excellent stability, which endow them with the potential to withstand harsh catalytic conditions [23], it is our hypothesis that bimetallic Zr-MOFs will have a combined benefit of stability and enhanced electronic behaviour.

Through metal-ion metathesis, post-synthetic exchange (PSE) has been applied to introduce new metal-ions into the secondary building units (SBUs) of MOFs while maintaining the framework's structural integrity [24,25]. The nature of the metal node of UiO-type MOFs, containing terminal μ_3-OH and μ_3-O allows PSE with a wide variety of metals [26]. Through PSE method, Li and co-workers [27] used 4 days to prepare Ti-substituted NH$_2$-UiO-66(Zr/Ti). PSE has been reported as one of the common techniques to construct bimetallic MOFs, which are efficient for photocatalysis [28]. *De novo* method is another approach for fabricating double metal containing MOFs. Assembling framework components by *de novo* synthetic approaches has been associated with multiple challenges such as unwanted competition among reactants, yield of fragile frameworks and formation of undesirable phases or amorphous by-products [29]. In MOFs synthesis, modulators such as acetic acid and benzoic acid act as regulator for the reaction rate and the crystal morphology [30]. Attempt by Schaate et al. [31] to prepare monometallic MOF, Zr–tpdc, without a modulator failed (poorly crystalline material), however using five or more equivalent of benzoic acid resulted in the formation of highly crystalline Zr–tpdc and further makes the procedure reproducible.

Herein, we report a series of novel bimetallic Zr-based MOFs, NH$_2$-UiO-66(Zr/M) (where M is Fe, Co, or Cu), prepared via solvothermal *de novo* synthesis with the frameworks retaining their structural integrity, which was achieved by using benzoic acid as a modulator. This *de novo* approach required only cheap chemical without the application of extra external energy, thus the method is facile and cost effective. The NH$_2$-UiO-66(Zr/Cu) catalyst proves highly efficient for CO$_2$ reduction and H$_2$ generation under visible light irradiation. This is the first time of using Zr(IV)-O-Cu(I) clusters in MOFs for these applications. The examination of optical and photoelectrochemical properties revealed that their high performance was due to optimum bandgap with enhanced charge transfer efficiency. Thus, bandgap engineering via biametallic node is a potential strategy for enhancing photocatalysis.

2. Experimental section

2.1. Materials

2-aminoterephthalic acid (ATA) was purchased from Sigma-Aldrich. Zirconium(IV) chloride (ZrCl$_4$), iron(II) sulfate heptahydrate (FeSO$_4$·7H$_2$O) and copper(I) chloride (CuCl) were purchased from Merck. Dimethylformamide (DMF) and benzoic acid were purchased from Fisher Scientific. Cobalt(II) chloride hexahydrate (CoCl$_2$·6H$_2$O) was procured from Panreac Quimica S. A. Triethanolamine (TEOA), acetonitrile (MeCN) and methanol were obtained from Scharlab. All reagents and chemicals were purchased and used without further purification, and Milli-Q water having resistivity > 18.2 MΩ was employed when required throughout the experiments.

2.2. Synthesis of NH$_2$-UiO-66(Zr/M)

H$_2$ATA (217 mg, 1.2 mmol) in 40 mL DMF was transferred to a 150 mL Teflon-lined stainless-steel autoclave under constant stirring. ZrCl$_4$ (210 mg, 0.9 mmol) and CoCl$_2$·6H$_2$O (71 mg, 0.3 mmol) were added and the mixture was further stirred for at least 30 min to ensure a clear solution. Afterwards, benzoic acid (733 mg, 6 mmol, 5 equiv. with respect to ATA) and H$_2$O (43 μL, 2 equiv. with respect to ATA) were introduced to the mixed solution followed by heating in an oven at 120 °C for 48 h. The solution was cooled to room temperature at the rate of 10 °C/h. The resultant product was collected by filtration, washed thoroughly with DMF and methanol followed by drying in an oven overnight at 100 °C. The obtained sample was denoted as Zr/Co-ATA (where the linker 2-aminoterephthalate is denoted as ATA). Similar synthetic procedures were used for the preparation of Zr/Cu-ATA and Zr/Fe-ATA, except that the CoCl$_2$·6H$_2$O was replaced with CuCl (30 mg, 0.3 mmol) and FeSO$_4$·7H$_2$O (83 mg, 0.3 mmol) respectively. Also, NH$_2$-UiO-66(Zr) was prepared by similar procedure except that only ZrCl$_4$ (280 mg, 1.2 mmol) was used, without any additional inorganic salts and the obtained product was denoted as Zr-ATA.

2.3. Materials characterization

Powder X-ray diffraction (XRD) of Zr/M-ATA materials were collected using a Panalytical X'PertPro apparatus. The thermal stability of the samples was examined by NETZSCH, STA 449 F3 Jupiter instrument. The UV–visible absorption spectra were studied using Cary 5000 UV–VIS-NIR spectrophotometer equipped with an integrating sphere. The Kubelka–Munk (K-M) equation below was used to calculate the bandgaps.

$$F(R_\alpha) = \frac{(1 - R_\alpha)^2}{2R_\alpha} = \frac{K}{S} \tag{1}$$

where $F(R_\alpha)$ is the Kubelka-Munk function, $R_\alpha = R_{sample}/R_{reference}$, K and S are the molar absorption coefficient and the scattering coefficient of the materials, respectively. The optical band gap and absorption coefficient have been calculated by the following equation.

$$\alpha h\nu = c(h\nu - E_g)^n \tag{2}$$

where α is the linear absorption coefficient, hν photon energy, C proportionality constant, E$_g$ optical band gap and n is a constant showing possible electronic transitions (n = 1/2 for direct allowed, n = 3/2 for direct forbidden, n = 2 for indirect allowed, and n = 3 for indirect forbidden). Here, n = 1/2 has been considered in Eq. (2), the final equation:

$$[F(R_\alpha)h\nu]^2 = c(h\nu - E_g) \tag{3}$$

Further characterization was carried out by scanning electron microscopy (SEM, Zeiss DSM 950) to check the samples' morphologies. The functionalities in the Zr/M-ATA were observed using attenuated total reflection Fourier transform infrared spectroscopy (ATR-FTIR, JASCO FT/IR-4600 spectrometer) in the 400–4000 cm^{-1} range. Photoluminescence (PL) measurements were acquired at room temperature using a LS50B Perking Elmer apparatus.

2.4. Photocatalytic CO$_2$ reduction

The photocatalytic test of the as-synthesized MOFs was conducted for CO$_2$ reduction. Freshly prepared MOFs were activated by heating at 100 °C for 12 h. 40 mg (23.36 μmol for Zr/Cu-ATA) of the activated MOFs was purged with CO$_2$. The sample was then added to a reactor containing a mixture of MeCN and TEOA (50 mL, v/v = 30:1), which has already been degassed with CO$_2$ to get rid of dissolved O$_2$. The reactor was further purged with CO$_2$ for 30 mins. Then, the solution was

irradiated with a Heraeus TQ Xe 150Xe-arc lamp with R3114 UV filter, < 3% transmission, producing light in the range of 420–800 nm. The reactions were performed under CO_2 atmosphere at ambient pressure and temperature. The light source was maintained at distance of 7 cm (corresponding to an irradiance of ~150 W.m^{-2}) from solution and cooling water circulation was used to ensure heat dissipation. The concentration of formate was detected by using a HPLC (Agilent 1200) with Kromasil 5 µm C18 column and 0.1 % H_3PO_4 (pH = 2) was used as eluent at a flow rate of 0.5 mL min^{-1}.

2.5. Photocatalytic H_2 generation

The photocatalytic H_2 generation with the as synthesized samples was assessed by water reduction at ambient temperature. A reactor (closed quartz cell) containing 1 mg·mL^{-1} MOFs concentration in a 30 mL solution with 25 vol% of methanol as sacrificial agent was irradiated with visible light (150 W Xenon lamp). Before the experiment, the solution was pre-gassed with argon for 15 min. Hydrogen production was followed by online gas chromatography (GC, Youngling, 3600).

2.6. Photoelectrochemical measurements

The photoelectrochemical properties of the synthesized materials were examined by preparing thin films on fluorine doped tin oxide (FTO) that was coated on a 2 cm × 2 cm glass slides by spin coating for 1 min at 4000 rpm. 100 µL of 2 mg·mL^{-1} catalyst's concentration in ethanol was employed for making each thin film layer. The FTO slides were three layers coated followed by drying for 2 h at a temperature of 200 °C.

A three-electrode quartz cell which contain**s** Na$_2$SO$_4$ (0.1 M ~ pH 7) electrolyte was used with KCl saturated Ag/AgCl as reference electrode and Pt wire as counter electrode. The studies were carried out in a galvanostat-potentiostat (PGSTAT302 N, Autolab, Metrohm) under 35 W Xenon lamp irradiation. The current density was measured between −0.4 V − 1 V (applied potential range) *vs* Ag/AgCl at 50 mV s^{-1} scanning rate through linear sweep voltammetry (LSV). Junction capacitance of the electrodes was measured at a frequency of 1000 Hz through Mott-Schottky (M-S) study to obtain the free charge carrier density and the flat band potentials. The potentials ($E_{Ag/AgCl}$) were converted to normal hydrogen electrode scale (E_{NHE}) using the Nernst equation as follows.

$$E_{NHE} = E_{Ag/AgCl} + 0.059 \times pH + 0.197 \tag{4}$$

3. Results and discussion

3.1. Catalyst characterization

The phase purity and local geometry of the NH$_2$-UiO-66(Zr/M) samples were studied by high-resolution powder X-ray diffraction (PXRD), Fig. 1a. All the diffraction peaks in the monometallic NH$_2$-UiO-66(Zr) sample corresponded well to simulated spectra [32], confirming the formation of pure crystalline phase. Therefore, its nodes consisted of Zr$_6$(µ$_3$-O)$_4$(µ$_3$-OH)$_4$(CO$_2$)$_{12}$ clusters with the Zr$_6$(µ$_3$-O)$_4$(µ$_3$-OH)$_4$ octahedron 12-fold bridged to adjacent Zr$_6$-octahedra through the linker [33]. Each Zr atom in the cluster was eight-coordinated with oxygen atoms emanating from -CO$_2$, µ$_3$-OH and µ$_3$-O groups (Fig. 1b) [34]. Moreover, the XRD pattern of Zr-ATA was similar to those of Zr/Fe-ATA, Zr/Cu-ATA and Zr/Co-ATA samples, suggesting that the structural integrity of the modified samples was preserved, meaning that they were isostructural. Closer observation of the XRD patterns of the samples at around 7.2–7.4° (2θ) showed that Zr/Cu-ATA has the least (2θ) value compared to other samples (Fig. 1a, inset). As usually reported for inorganic semiconductor solid solutions, this observation was attributed to the larger ionic radius of copper in the Cu-oxo cluster of Zr/Cu-ATA [35–37]. Overall, the presence of the secondary metal ions did not change the structure of the SBUs of the framework.

SEM was employed to examine the surface morphology of monometallic and the bimetallic frameworks. Fig. S1a (Supporting Information, SI) displays the octahedral geometry of bulk NH$_2$-UiO-66(Zr). Closer observation of this sample by magnifying the SEM image, Fig. S1b, revealed relatively uniform octahedral NH$_2$-UiO-66(Zr) nanocrystals with an average particle size in the 90–100 nm range [34]. The SEM image of Zr/Cu-ATA shows that incorporating the secondary metal did not have significant effect on the structure, thus the octahedral morphology and crystal size (Zr/Cu-ATA around 90 nm) were preserved (Fig. S1c and Fig. S1d). Normally, the concentration of amine moieties influences the crystal evolution and structures of UiO-66 type MOFs [34]. However, the amine content was the same for the four Zr/M-ATA MOFs with only H$_2$ATA as the organic ligand, thereby resulting in non-significant alteration of structure and morphology. Furthermore, homogenous octahedral morphology with similar particle size was revealed in the SEM image of Zr/Fe-ATA and Zr/Co-ATA, as illustrated in Fig. S1e and Fig. S1f, respectively.

Fig. S2 represents the Fourier transform infrared (FTIR) spectra of the ligand and the synthesized MOFs. These spectra were used to examine the available functionalities in the MOFs and to assess whether the ligands were coordinated to the metal ion during the synthesis. Two peaks of symmetric (3387 cm^{-1}) and asymmetric (3490 cm^{-1})
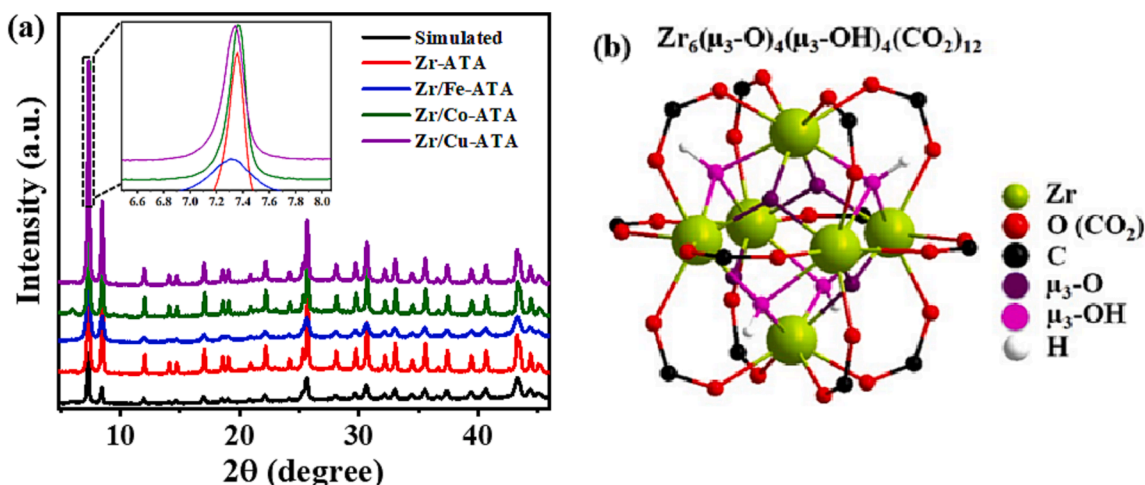

Fig. 1. XRD diffraction of NH$_2$-UiO-66(Zr/M) samples (a) and Zr$_6$(µ$_3$-O)$_4$(µ$_3$-OH)$_4$(CO$_2$)$_{12}$ metal clusters (b).

stretching vibration of the primary NH$_2$ group were clearly observed in the spectra of ligand and MOFs [38]. Therefore, the amine group was free after MOFs' formation, which agrees with the XRD results. For H$_2$ATA, an absorption peak observed at 1681 cm^{-1} is due to the ν(C=O) stretching vibration of uncoordinated –COOH. This peak was absent from the FTIR of the MOFs, showing the deprotonation of the carboxylic acid group during MOFs synthesis. Furthermore, the new peak at 1653 in MOF spectra, is due to the antisymmetric stretching vibration of the deprotonated carboxylic group [39], which confirmed the coordination between the amine-based ligand and Zr/M ions for the formation of the bimetallic frameworks. In the lower frequency region, the peak of C-N stretching of the aromatic amine is observed at 1256 cm^{-1} [34]. The appearance of sharp characteristic peak at 1378 cm^{-1} is due to the stretching of C=C in the amino terephthalate linker of the MOFs. The bands <917 cm^{-1} are assigned to the C–H bond and the C=C–H of the benzene rings [40,41].

The thermal stability of the bimetallic NH$_2$-UiO-66(Zr/M) samples was examined by TGA, and DSC analyses from 25 to 800 °C as illustrated in Fig. S3. The first total weight loss of 5.4 % was detected at the temperature range 47.7–107.5 °C with an exothermic DSC peak at 65 °C attributed to the removal of coordinated water molecules and methanol [42]. Further heating resulted in weight losses around 200 °C assigned to the removal of occluded DMF molecules in the pores of the frameworks. The remaining DMF, 4.1 %, was released in the 238–279 °C range with small exothermic peaks observed at 275.4 °C [43]. The frameworks collapsed at 470 °C with a total weight loss of 37.5 %. Notably, the thermal stability of the monometallic MOFs, Zr/Co-ATA and Zr/Cu-ATA were similar, meaning that the incorporation of secondary metal ions did not impair the stability of the bimetallic frameworks. Zr/Fe-ATA even displayed a higher thermal stability than monometallic MOFs. Moreover, Zr/Fe-ATA recorded the highest thermal stability compared to the other bimetallic frameworks, which may be due to the higher electro-positivity of Fe(II), resulting in a stronger bond [44]. The CO$_2$ adsorption isotherm of the prepared samples at 1 atm and 273 K, as illustrated in Fig. S4, revealed that Zr-ATA has a maximum CO$_2$ uptake of 110 cm^3 g^{-1}. Among the bimetallic MOFs, Zr/Cu-ATA shows the highest CO$_2$ adsorption capacity of 76 cm^3 g^{-1}, while that for Zr/Co-ATA and Zr/Fe-ATA are 56 and 28 cm^3 g^{-1}, respectively. The nominal amount of the secondary metals (Cu, Fe, and Co) incorporated into the bimetallic frameworks is 7.0 wt%.

The permanent porosity and architectural stability of the frameworks were confirmed by N2 adsorption. The corresponding BET and Langmuir surface areas of Zr-ATA, Zr/Co-ATA, Zr/Fe-ATA, and Zr/Cu-ATA are 956.96 and 1120.86 m^2/g, 967.51 and 1135.62 m^2/g, 958.77 and 1129.33 m^2/g, and 981.54 and 1175.61 m^2/g, respectively. There is observed little increase the surface area of the bimetallic frameworks compared with the monometallic MOFs, which may be attributed to the

atomic size of the incorporated secondary metal.

3.2. UV–Vis and photoluminescence analysis

The UV–Vis absorption spectra of the samples are presented in Fig. 2a, where ligand showed an absorption peak centered at 375 nm, which became wider after monometallic Zr-MOF formation. Interestingly, when the Zr is modified with other metals (Fe, Cu, Co), the absorption shape modified, the peak maxima shifted to the visible region and the absorption extended from UVA to the near-IR region. The 60 nm bathochromic shift and secondary absorption peak at 810 nm, due to surface plasmon resonance (SPR) effect [45], was observed specifically for Zr/Cu-ATA. This observation strongly suggested that bimetallic MOF structures involving d-transition metals have intermetallic mechanism to effectively enhance solar energy absorption in the visible and near-IR region. The relevant bandgaps of ligand and MOFs have been calculated from the K−M equation [45] as illustrated by Tauc plots in Fig. 2b.

The calculated bandgaps were 3.06 eV, 2.95 eV, 2.66 eV, 1.93 eV and 2.62 eV for ligand (H$_2$ATA), Zr-ATA, Zr/Fe-ATA, Zr/Cu-ATA and Zr/Co-ATA, respectively. Therefore, it has been clearly revealed that bandgap values are effectively narrowed, which refers to the improvement of visible light absorption [46]. A significant reduction in the bandgap values for Zr/Fe-ATA, Zr-Cu/ATA and Zr/Co-ATA compared to Zr-ATA might be attributed to the combination of two metal cations in the earlier MOF structure [47].

Photoluminescence spectroscopy (PL) is a reliable means of examining electron-transfer process in MOFs. The PL analysis was conducted on the organic ligand, H$_2$ATA, and the MOF materials to elucidate the photoinduced charge transfer process taking place in the frameworks (Fig. 4a and Fig. 4b). Previous reports revealed that under light irradiation, excited electron can be transferred from the amine linkers to the Zr-oxo clusters, via ligand-to-metal charge-transfer (LMCT). As observed in Fig. 3a, H2ATA showed broad asymmetric emission band from 400 to 620 nm, with a maximum centered at 530 nm, where the resolved fine structure allows to identify two shoulders at 485 nm and 460 nm, which may be assigned to n-π* transition of lone pair of electrons from the –NH$_2$ moieties. Regarding MOFs, a single and narrower emission peak blue-shifted to 450 nm was observed in mono- and bi-metallic MOFs, with the only exception of Zr/Fe-ATA, which showed a minor luminescence signal at 475 nm. The emission bands observed in the framework materials can be ascribed to the transfer of electron from the amine-based linker to the metal-oxo clusters [48,49].

In order to ascertain the exact electronic transition and the origin of the luminescence emission at 450 nm, the excitation spectra of MOFs and the linker at this particular wavelength were obtained. As illustrated in Fig. 3b, no PL excitation band was observed for the pure linker and Zr/Fe-ATA, probably due to the short-range connections in the 3D
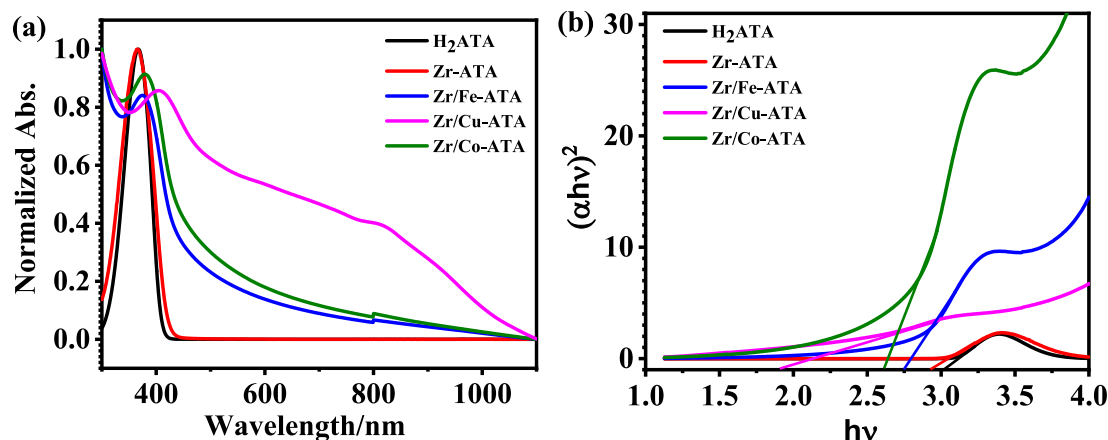

Fig. 2. UV–Vis absorption spectra of the ligand and MOF samples (a) and Kubelka–Munk plot of the samples for band gap calculations (b).
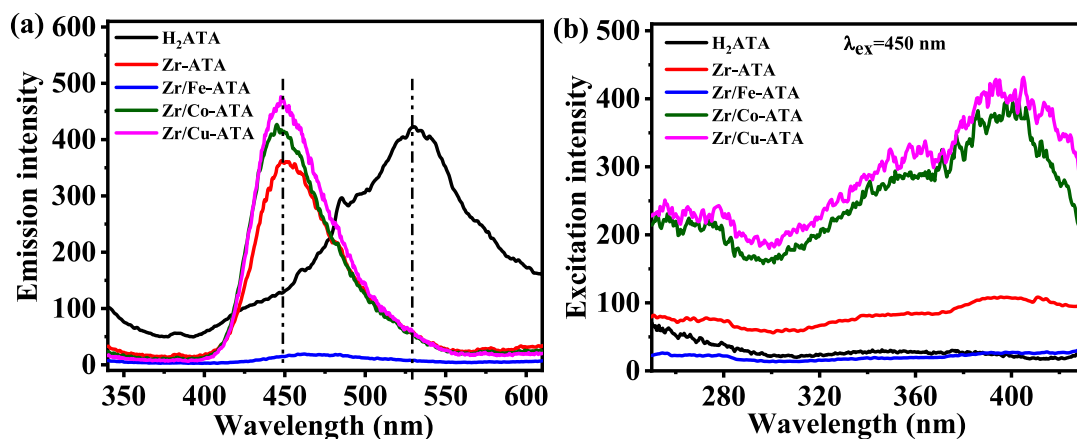
Fig. 3. Photoluminescence emission spectra of the H$_2$ATA and Zr/M-ATA at 320 nm excitation wavelength (a) and excitation spectra corresponding to the emission signals at 450 nm wavelength (b).
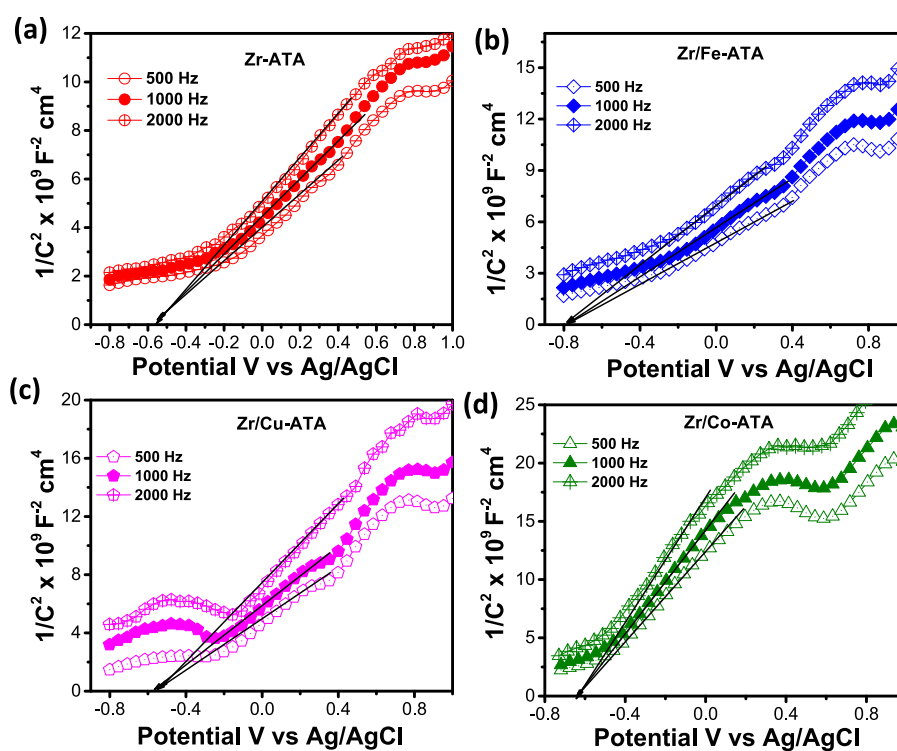

Fig. 4. Mott-Schottky plots of pure semiconductors Zr-ATA (a), Zr/Fe-ATA (b), Zr/Cu-ATA (c) and Zr/Co-ATA MOFs (d).

network developed in this MOF as pointed in XRD results (Fig. 1, inset). Moreover, Zr/Co-ATA and Zr/Cu-ATA showed three peaks at about 400 nm, 355 nm, and 275 nm. The high intensity band at 400 nm may be due to the local excitation of the amine linker [50]. The strong Lewis acidic nature of Zr(IV) enhanced the electron withdrawal from the linker, which can be the origin of the peak at 355 nm [50].

Also, the weak absorption band at 275 nm was attributed to the secondary metal ion at the node and the peak assigned to the Zr-oxo-M electron transfer. These three bands could be hardly distinguished in the monometallic Zr-ATA MOF. Excitation PL spectra for 530 nm emission peak (Fig. S5) show very similar signals for the linker and all the MOFs with lower intensity for bimetallic Zr/M-ATA, which assess the lower charge transitions allowed at this wavelength [49].

3.3. Semiconductor properties

The semiconductor character of the MOFs and its photocatalytic capacity under visible light illumination was assessed using M-S measurements at 1000 Hz (Fig. 4). All MOFs exhibit positive slope in C^{-2} *vs.* applied potentials plots, which is characteristic from n-type semiconductors [51]. The flat band potentials (E$_{fb}$) were determined from the intersection at C^{-2} = 0, yielding –0.48 V, –0.78 V, –0.50 V and –0.43 V *vs.* Ag/AgCl for Zr-ATA, Zr/Fe-ATA, Zr/Cu-ATA and Zr/Co-ATA, respectively. Therefore, by using the Nernst equation, the E$_{fb}$ values were 0.13 V, –0.17 V, 0.11 V, 0.18 V *vs.* NHE for Zr-ATA, Zr/Fe-ATA, Zr/Cu-ATA and Zr/Co-ATA, respectively. It is known that the E$_{fb}$ potential in n-type semiconductors is closely near to the bottom of the conduction band (CB = E$_{fb}$ − 0.2 V) [52]. Thus, the LUMO of Zr-ATA, Zr/Fe-ATA, Zr/Cu-ATA and Zr/Co-ATA are estimated to be –0.07 V, –0.37 V, –0.09 V, –0.02 V *vs.* NHE, respectively. The HOMO of MOFs would be 2.88 V,

2.29 V, 1.84 V and 2.60 V for Zr-ATA, Zr/Fe-ATA, Zr/Cu-ATA and Zr/Co-ATA, respectively using their bandgap values (VB − CB = E_g) [53]. The E_{fb}, HOMO, LUMO and the E_g potentials for the MOFs prepared in this work are presented in Table S2.

Depending on the HOMO and LUMO potentials, the band structures of the MOFs are presented in Scheme 1.

Furthermore, charge carrier concentration of the MOFs was calculated using the following equation:

$$\frac{1}{C_{sc}^2} = \frac{2}{eN_d\varepsilon\varepsilon_0}\left(E - E_{fb} - \frac{KT}{E}\right) \tag{5}$$

where, C_{SC} is the space charge capacitance that occurs at the junction interface (F cm^{-2}), e is the charge of electron (C), N_d is free charge carrier density (cm^{-3}), E_{fb} is flat band potential (V), ε is dielectric constant of MOF (2.33), ε_0 is permittivity of free space, T is temperature (K) and K is Boltzmann constant.

3.4. Photocatalytic CO₂ reduction performance

The catalytic performance of the as-synthesized MOFs was examined for CO_2 reduction under visible light irradiation. Photocatalytic Zr-based MOFs have been reported to selectively convert CO_2 to formate anions in a mixed solution of triethanolamine (TEOA) and acetonitrile (CH_3CN) [54]. In that case, TEOA act as a sacrificial electron donor and proton donor and further provides the required alkaline medium necessary for CO_2 reduction [55]. CH_3CN presents good solubility for CO_2 due to its cation-solvating capacity, thereby facilitating charge transfer to CO_2 [54]. Therefore, the photocatalytic experiments were conducted in a customized glass system under visible light irradiation for a duration of 10 h. As shown in Fig. 5, the monometallic MOF, Zr-ATA, can catalytically reduce CO_2, generating 15.7 µmol of formate in 10 h, which is similar to the yield reported elsewhere [50]. Our results showed that the bimetallic frameworks Zr/Fe-ATA, Zr/Co-ATA and Zr/Cu-ATA outperform the monometallic one. Thus, the incorporation of the secondary metal ions i.e., M-oxo clusters, can favour the transfer of electron from the excited linker to the Zr-O clusters, [37] and also it can reduce the bandgap, which enhanced the overall photocatalytic activities. The cumulative amount of generated HCOO⁻ continued to increase after 10 h of maintained experiment. Fig. 5 further revealed that Zr/Cu-ATA had the highest catalytic performance, generating up to 28.68 µmol of HCOO⁻ in 10 h with an estimated average formate formation rate of
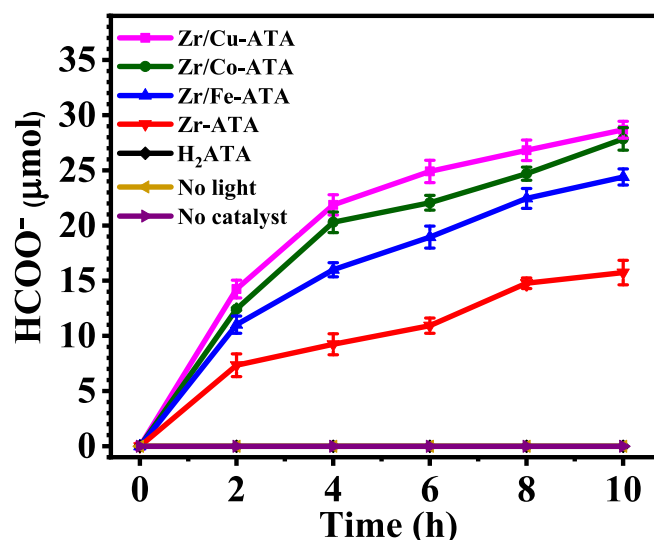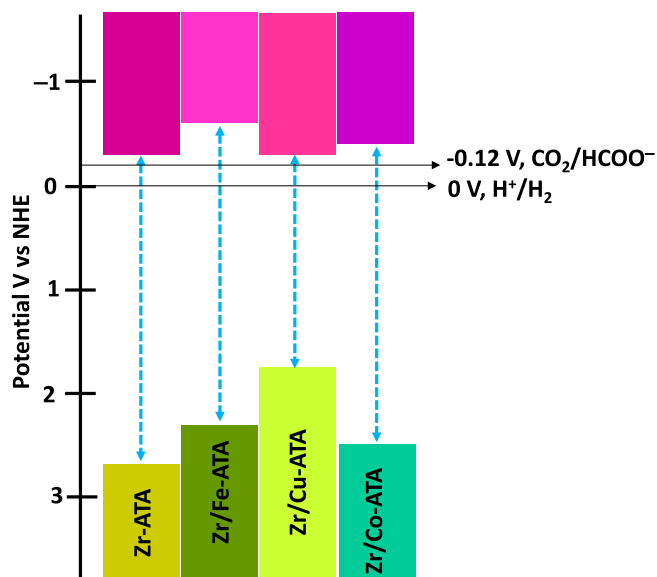

Fig. 5. Time-evolution of photocatalytic CO_2 reduction with mono- and bimetallic MOFs. Blank experiments have been included for reference. The solutions were irradiated with a Xe-arc lamp with filter to produce light in the range 420–800 nm. MeCN/TEOA (30:1, v/v), photocatalysts: 40 mg, solution volume: 50 mL. Error bars represent the standard deviation for a sample size of n = 3.

122 µmol h^{-1} mmol$_{MOF}^{-1}$, which is recorded among the highest performance of NH₂-UiO-66 based MOFs, as illustrated in Table S1. The best photocatalytic activity of this sample may be attributed to the enhanced light absorption and optimized bandgap, which is in accordance with the UV–Vis, PL and Mott-Schottky analyses. The reusability evaluation of Zr/Cu-ATA shows that the recollected sample conserved a good CO_2 photoreduction performance after three cycle of reuse, Fig. S6. The powder XRD profile (Fig. S8) and the FTIR spectra (Fig. S9) did not show significant changes after the reactions, revealing that the crystal structure and the functionalities of the frameworks are retained, respectively. To further study the stability of the Zr/Fe-ATA photocatalyst, the water stability was evaluated by contacting the material with ultrapure water at ambient temperature for 24 h. Subsequently, the XRD result, Fig. S8, revealed that the MOFs retained its crystalline structure, thus the framework is water stable, which is attributed to its structured formed by 12-connected Zr₆ clusters [23].

3.5. Evaluation of photocatalytic H₂ generation

The data presented in Table S2 show that all the MOFs have sufficiently negative LUMO potential relative to the water reduction reaction (0 V *vs*. NHE, H⁺/H₂); indicating that the as-developed MOFs were theoretically suitable for photocatalytic hydrogen generation through water reduction. The hydrogen generation reactions were evaluated under visible light irradiation, Fig. 6. The hydrogen generation of ligand H₂ ATA was very low (~4.9 mmol.g⁻¹) because of poor visible light absorption. Interestingly, the amount of hydrogen generation significantly increased after incorporation of metals *via* MOF formation. Analogously to the previous CO_2 photoreduction results, Zr/Cu-ATA exhibits the highest amount of hydrogen generation (~12.8 mmol.g⁻¹ in 120 min) compared to the other prepared MOFs, which was attributed to their narrow band gap and better charge transfer efficiency. Furthermore, the recycling data for photocatalytic H₂ generation has been studied and only 12% loss observed after fourth cycle, Fig. S7. Therefore, it can be concluded that, as prepared MOFs can be reused for photocatalytic reaction.

Scheme 1. Band diagrams of the Zr-ATA, Zr/Fe-ATA, Zr/Cu-ATA and Zr/Co-ATA MOFs.
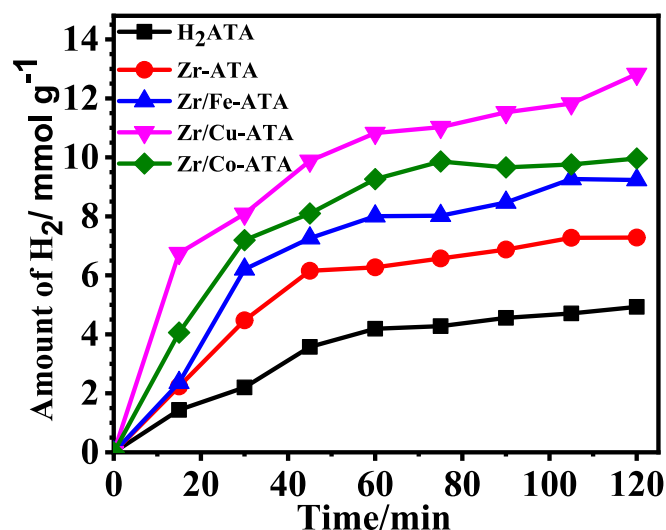
Fig. 6. Time-evolution of visible-light-driven photocatalytic hydrogen generation capacities of samples in 25 vol% MeOH as sacrificial agent at pH 7.

3.6. Photoelectrochemical properties

To further ascertain the reason for the higher photocatalytic performance of bimetallic MOFs compared to the monometallic one, their photoelectrochemical activities were measured through LSV under continuous visible light illumination in a three-electrode cell containing 0.1 M Na_2SO_4 electrolyte. Fig. 7a shows the LSV plots for ligand and MOFs, showing three-fold current density increase after MOF formation (Zr-ATA) compared to the ligand H2ATA. Interestingly, Zr/Cu-ATA displayed very high current density of ~83 $\mu A \cdot cm^{-2}$ compared to the other MOFs, which was indicative of higher photoreduction efficiency. Similar trend has been observed for chronoamperometry under light

on–off experiment, Fig. 7b. The results for photocurrent density strongly suggest that the bimetallic MOFs have higher current density than the monometallic one. The electrochemical impedance measurements presented in Fig. 7c is used to check the efficiency of charge transfer of the samples at the elect rode-electrolyte interface. The MOFs show a semicircle for high frequency, small Warburg line at medium frequency and nearly a vertical line in the lower region of the frequency.

The semicircular sections are due to the transfer of electron between the redox active species and the electrode through the reaction intermediates or surface states and the steep parts correspond to the diffusion of redox active species, which agrees with the electrode's capacitive nature. All the MOFs showed very low charge transfer resistance compared to the ligand (~1700 Ω), the smaller resistance observed for Zr/Cu-ATA and Zr/Co-ATA MOFs (~42 Ω). Thus, it can be concluded that, significant improvement has been obtained in the electrical conductivity at the electrode-electrolyte interface after MOF functionalization (of the electrode). Therefore, these results show that rational design of bimetallic frameworks is a strategy of taking advantage of the synergistic contribution of the two metals to enhance CO_2 reduction and H_2 generation under visible light irradiation.

3.7. Mechanism for photoreduction reactions

Based on the above observations, a proposed charge transfer mechanism for the photoreduction reaction over NH_2-UiO-66(Zr/Cu) can be discussed concisely as follows, Scheme 2. Fundamentally, CO_2 photoreduction is a multistep process that involves CO_2 adsorption on the framework material, activation, and dissociation of the C-O bond [11]. Regarding the previous report on photocatalytic CO_2-to-$HCOO^-$ conversion over the monometallic MOFs, NH_2-UiO-66(Zr), upon irradiation of visible light, the linker (ATA) is excited followed by electron transfer from the excited ATA to the Zr–O clusters through the ligand-to-metal charge transfer (LMCT) process, thereby reducing Zr(IV) to Zr(III) [50]. Then, the activated Zr(III) donate the required electron for the reduction reaction. In this work, since NH_2-UiO-66(Zr/Cu) is bimetallic,
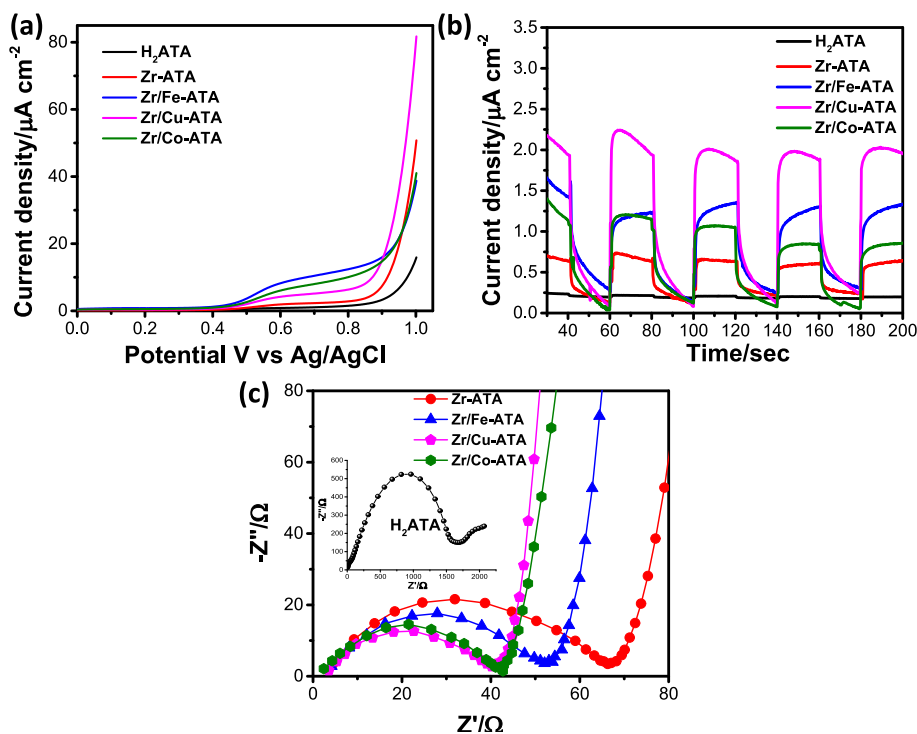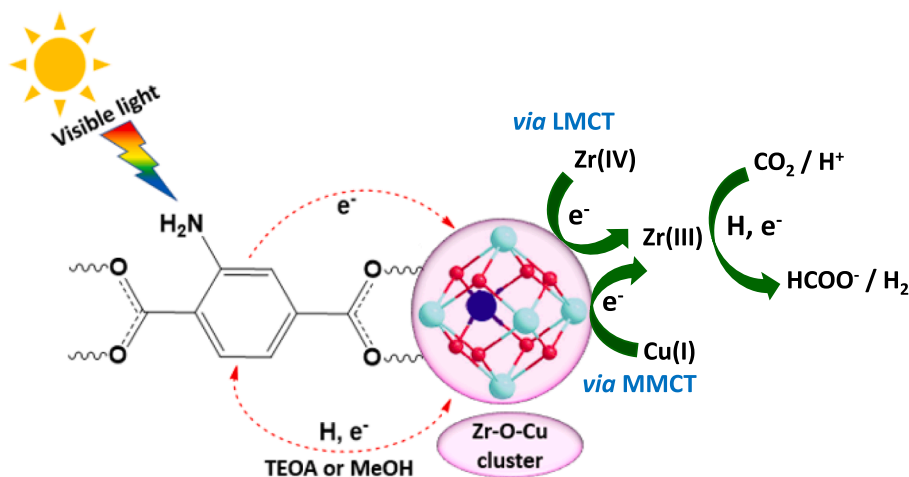

Fig. 7. (a) Linear sweep voltammetry (LSV), (b) Chopped chronoamperometry and The LSV was taken in 0.1 M Na_2SO_4 electrolyte under continuous visible light illumination. (c) Electrochemical impedance spectra of ligand and as-prepared MOFs in 0.1 M Na_2SO_4 electrolyte. Inset (c): Impedance spectra of ligand (2-aminoterephthalic acid, ATA).

Scheme 2. Proposed mechanism for the visible light photocatalytic reactions over NH$_2$-UiO-66(Zr/Cu).

the excited ATA transfers electrons to the Zr(IV)-O-Cu(I) clusters via the LMCT. Zr oxo-bridged to a Cu(I) center, was previously observed on the pore surface of silicate sieve [56]. Similarly, Sun et al. and Nakamura et al. reported oxo-bridged Zr(IV)-O-Ti(III) and Ti(III)-O-Ce(III) respectively [27,57]. In the activated bimetallic clusters, electrons would be transferred from Cu(I) to the Zr(IV) by oxo-bridged metal-to-metal charge transfer (MMCT), thereby resulting in the formation of Zr(III)−O−Cu(II) sites. In Cu(I) containing bimetallic system, such as Ti(IV)-O-Cu(I), the Cu(I) acts as electron donor during the MMCT process [56,58]. The reduction reactions of CO$_2$ and H$_2$O occur at the.

MMCT-excited Zr(III) center, via the valence change from Zr(IV) to Zr(III), which is the active site for the reduction reaction, Scheme 2. Therefore, the Cu sites in the bimetallic NH$_2$-UiO-66(Zr/Cu) frameworks is beneficial to improve the charge transfer efficiency, thus enhancing the overall visible light photocatalysis.

4. Conclusions

In summary, we prepared a series of bimetallic amine-based MOFs, Zr/Fe-ATA, Zr/Co-ATA and Zr/Cu-ATA by *de novo* synthetic approach to circumvent the time and energy intensive post-synthetic metal exchange method. Spectroscopic and microscopic analyses of the bimetallic frameworks revealed that their crystal structure, morphology, and stability were not affected by the incorporation of the secondary metal ion. Evaluation of the visible-light-driven CO$_2$ reduction and H$_2$ generation performance demonstrated that Zr/Fe-ATA, Zr/Co-ATA and Zr/Cu-ATA outperformed the monometallic Zr-ATA frameworks. Moreover, NH$_2$-UiO-66(Zr/Cu) (sample Zr/Cu-ATA) had the highest capacity for CO$_2$ reduction to formate (28.68 μmol in 10 h) and H$_2$ generation (12.8 mmol in 2 h), compared to other prepared bimetallic MOFs. Interestingly, the estimated average formation rate of HCOO$^-$ is 122 μmol h^{-1} mmol$_{MOF}^{-1}$, which is among the highest for NH$_2$-UiO-66 based MOFs. The results from the spectroscopic and photoelectrochemical analyses revealed that the high catalytic performance of NH$_2$-UiO-66(Zr/Cu) can be attributed to its narrow bandgap, higher charge transfer efficiency and the availability of large number of active sites. Therefore, rational design of bimetallic frameworks are promising strategy to enhance artificial photosynthesis.

CRediT authorship contribution statement

Chizoba I. Ezugwu: Formal analysis, Funding acquisition, Investigation, Writing – original draft, Writing – review & editing. **Srabanti Ghosh:** . **Susmita Bera:** . **Marisol Faraldos:** Formal analysis. **Marta E. G. Mosquera:** . **Roberto Rosal:** Supervision, Funding acquisition.

Declaration of Competing Interest

The authors declare that they have no known competing financial interests or personal relationships that could have appeared to influence the work reported in this paper.

Data availability

Data will be made available on request.

Appendix A. Supplementary data

Supplementary data to this article can be found online at https://doi.org/10.1016/j.seppur.2022.122868.

References

[1] M.D. Garba, M. Usman, S. Khan, F. Shehzad, A. Galadima, M.F. Ehsan, A. S. Ghanem, M. Humayun, CO$_2$ towards fuels: A review of catalytic conversion of carbon dioxide to hydrocarbons, J. Environ. Chem. Eng. 9 (2021) 104756.

[2] V.-H. Nguyen, B.-S. Nguyen, Z. Jin, M. Shokouhimehr, H.W. Jang, C. Hu, P. Singh, P. Raizada, W. Peng, S.S. Lam, C. Xia, C.C. Nguyen, S.Y. Kim, Q.V. Le, Towards artificial photosynthesis: Sustainable hydrogen utilization for photocatalytic reduction of CO$_2$ to high-value renewable fuels, Chem. Eng. J. 402 (2020) 126184.

[3] T.-C. Li, X.-J. Kong, Y. Xie, T. He, G.-R. Si, X.-Y. Li, W. Wu, M. Zhao, J.-R. Li, Metalloporphyrin functionalized multivariate IRMOF-74-IV analogs for photocatalytic CO$_2$ reduction, Sep. Purif. Technol. 292 (2022) 121080.

[4] S. Ghosh, N.A. Kouamé, L. Ramos, S. Remita, A. Dazzi, A. Deniset-Besseau, P. Beaunier, F. Goubard, P.-H. Aubert, H. Remita, Conducting polymer nanostructures for photocatalysis under visible light, Nat. Mater. 14 (2015) 505–511.

[5] S. Bera, A. Kumari, S. Ghosh, R.N. Basu, Assemble of Bi-doped TiO$_2$ onto 2D MoS$_2$: an efficient p–n heterojunction for photocatalytic H$_2$ generation under visible light, Nanotechnology 32 (2021) 195402.

[6] S. Bera, S. Ghosh, R.N. Basu, Fabrication of Bi$_2$S$_3$/ZnO heterostructures: an excellent photocatalyst for visible-light-driven hydrogen generation and photoelectrochemical properties, New J. Chem. 42 (2018) 541–554.

[7] S. Mubarak, D. Dhamodharan, H.-S. Byun, D.K. Pattanayak, E. Arya, Efficient photoelectrocatalytic conversion of CO$_2$ to formic acid using Ag-TiO$_2$ nanoparticles formed on the surface of nanoporous structured Ti foil, J. Ind. Eng. Chem. 113 (2022) 124–131.

[8] Y. Wang, H. Wang, H. He, Study on nanoporous CuBi$_2$O$_4$ photocathode coated with TiO$_2$ overlayer for photoelectrochemical CO$_2$ reduction, Chemosphere 264 (2021) 128508.

[9] Q. Chen, X. Lan, K. Chen, Q. Ren, J. Shi, Construction of WO$_3$/CsPbBr 3 S-scheme heterojunction via electrostatic Self-assembly for efficient and Long-Period photocatalytic CO2 reduction, J. Colloid Interface Sci. 616 (2022) 253–260.

[10] Y. Shi, A.-F. Yang, C.-S. Cao, B. Zhao, Applications of MOFs: Recent advances in photocatalytic hydrogen production from water, Coord. Chem. Rev. 390 (2019) 50–75.

[11] C.I. Ezugwu, S. Liu, C. Li, S. Zhuiykov, S. Roy, F. Verpoort, Engineering metal-organic frameworks for efficient photocatalytic conversion of CO₂ into solar fuels, Coord. Chem. Rev. 450 (2022) 214245.

[12] S. Padmanaban, M. Kim, S. Yoon, Acid-mediated surface etching of a nano-sized metal-organic framework for improved reactivity in the fixation of CO₂ into polymers, J. Ind. Eng. Chem. 71 (2019) 336–344.

[13] M. Usman, Z. Zeb, H. Ullah, M.H. Suliman, M. Humayun, L. Ullah, S.N.A. Shah, U. Ahmed, M. Saeed, A review of metal-organic frameworks/graphitic carbon nitride composites for solar-driven green H₂ production, CO₂ reduction, and water purification, J. Environ. Chem. Eng. 10 (2022) 107548.

[14] Z. Xu, X. Deng, Y. Chen, J. Wen, L. Shi, Z. Bian, Engineering a Rapid Charge Transfer Pathway for Enhanced Photocatalytic Removal Efficiency of Hexavalent Chromium over C₃N₄/NH₂–UiO–66 Compounds, Sol. RRL 5 (2021) 2000416.

[15] R.R. Ikreedeegh, M. Tahir, Indirect Z-scheme heterojunction of NH₂-MIL-125 (Ti) MOF/g-C₃N₄ nanocomposite with RGO solid electron mediator for efficient photocatalytic CO₂ reduction to CO and CH₄, J. Environ. Chem. Eng. 9 (2021) 105600.

[16] C.H. Hendon, D. Tiana, M. Fontecave, C.m. Sanchez, L. D'arras, C. Sassoye, L. Rozes, C. Mellot-Draznieks, A. Walsh, Engineering the optical response of the titanium-MIL-125 metal–organic framework through ligand functionalization, J. Am. Chem. Soc. 135 (2013) 10942–10945.

[17] D. Li, M. Kassymova, X. Cai, S.-Q. Zang, H.-L. Jiang, Photocatalytic CO2 reduction over metal-organic framework-based materials, Coord. Chem. Rev. 412 (2020) 213262.

[18] C.I. Ezugwu, J.M. Sonawane, R. Rosal, Redox-active metal-organic frameworks for the removal of contaminants of emerging concern, Sep. Purif. Technol. 284 (2021) 120246.

[19] R. Gaikwad, S. Gaikwad, S. Han, Bimetallic UTSA-16 (Zn, X; X= Mg, Mn, Cu) metal organic framework developed by a microwave method with improved CO₂ capture performances, J. Ind. Eng. Chem. 111 (2022) 346–355.

[20] K. Loza, M. Heggen, M. Epple, Synthesis, structure, properties, and applications of bimetallic nanoparticles of noble metals, Adv. Funct. Mater. 30 (2020) 1909260.

[21] M. Siegert, J.M. Sonawane, C.I. Ezugwu, R. Prasad, Economic assessment of nanomaterials in bio-electrical water treatment, in: Advanced Research in Nanosciences for Water Technology, Springer, 2019, pp. 1-23.

[22] X. Yang, P. Pachfule, Y. Chen, N. Tsumori, Q. Xu, Highly efficient hydrogen generation from formic acid using a reduced graphene oxide-supported AuPd nanoparticle catalyst, Chem. Commun. 52 (2016) 4171–4174.

[23] L. Valenzuela, G. Amariei, C.I. Ezugwu, M. Faraldos, A. Bahamonde, M. E. Mosquera, R. Rosal, Zirconium-based Metal-Organic Frameworks for highly efficient solar light-driven photoelectrocatalytic disinfection, Sep. Purif. Technol. 285 (2021) 120351.

[24] A. Bagheri, H. Hoseinzadeh, B. Hayati, N.M. Mahmoodi, E. Mehraeen, Post-synthetic functionalization of the metal-organic framework: Clean synthesis, pollutant removal, and antibacterial activity, J. Environ. Chem. Eng. 9 (2021) 104590.

[25] C.I. Ezugwu, O.T. Ujam, P.O. Ukoha, N.N. Ukwueze, Complex Formation and Extraction Studies of N, N¢-Bis (salicylidene)-3, 5-diaminobenzoic Acid on Hg (II) and Ag (I), Chem. Sci. Trans. 2 (2013) 1118–1125.

[26] D.R. Pahls, M.A. Ortuño, P.H. Winegar, C.J. Cramer, L. Gagliardi, Computational screening of bimetal-functionalized Zr₆O₈ MOF nodes for methane C-H bond activation, Inorg. Chem. 56 (2017) 8739–8743.

[27] D. Sun, W. Liu, M. Qiu, Y. Zhang, Z. Li, Introduction of a mediator for enhancing photocatalytic performance via post-synthetic metal exchange in metal–organic frameworks (MOFs), Chem. Commun. 51 (2015) 2056–2059.

[28] M. Kalaj, S.M. Cohen, Postsynthetic modification: an enabling technology for the advancement of metal–organic frameworks, ACS Cent. Sci. 6 (2020) 1046–1057.

[29] O. Karagiaridi, W. Bury, J.E. Mondloch, J.T. Hupp, O.K. Farha, Solvent-assisted linker exchange: an alternative to the de novo synthesis of unattainable metal–organic frameworks, Angew. Chem. Int. Ed. 53 (2014) 4530–4540.

[30] T. Tsuruoka, S. Furukawa, Y. Takashima, K. Yoshida, S. Isoda, S. Kitagawa, Nanoporous nanorods fabricated by coordination modulation and oriented attachment growth, Angew. Chem. 121 (2009) 4833–4837.

[31] A. Schaate, P. Roy, A. Godt, J. Lippke, F. Waltz, M. Wiebcke, P. Behrens, Modulated synthesis of Zr-based metal-organic frameworks: from nano to single crystals, Chem. Eur. J. 17 (2011) 6643–6651.

[32] H. Molavi, A. Eskandari, A. Shojaei, S.A. Mousavi, Enhancing CO₂/N₂ adsorption selectivity via post-synthetic modification of NH₂-UiO-66 (Zr), Microporous Mesoporous Mater. 257 (2018) 193–201.

[33] G.C. Shearer, S. Chavan, J. Ethiraj, J.G. Vitillo, S. Svelle, U. Olsbye, C. Lamberti, S. Bordiga, K.P. Lillerud, Tuned to perfection: ironing out the defects in metal–organic framework UiO-66, Chem. Mater. 26 (2014) 4068–4071.

[34] C.I. Ezugwu, S. Zhang, S. Li, S. Shi, C. Li, F. Verpoort, J. Yu, S. Liu, Efficient transformative HCHO capture by defective NH2-UiO-66(Zr) at room temperature, Environ. Sci.: Nano 6 (2019) 2931–2936.

[35] Y.-F. Li, D. Xu, J.I. Oh, W. Shen, X. Li, Y. Yu, Mechanistic study of codoped titania with nonmetal and metal ions: a case of C+ Mo codoped TiO₂, ACS Catal. 2 (2012) 391–398.

[36] C. Artner, A. Koyun, U. Schubert, A heterobimetallic copper–titanium oxo cluster with a new structural motif, Monatsh. Chem. 146 (2015) 1777–1780.

[37] A. Santiago Portillo, H.G. Baldoví, M.T. Garcia Fernandez, S. Navalon, P. Atienzar, B. Ferrer, M. Alvaro, H. Garcia, Z. Li, Ti as mediator in the photoinduced electron transfer of mixed-metal NH₂–UiO-66 (Zr/Ti): transient absorption spectroscopy study and application in photovoltaic cell, J. Phys. Chem. 121 (2017) 7015–7024.

[38] N. Rabiee, M. Bagherzadeh, M. Heidarian Haris, A.M. Ghadiri, F. Matloubi Moghaddam, Y. Fatahi, R. Dinarvand, A. Jarahiyan, S. Ahmadi, M. Shokouhimehr, Polymer-Coated NH2-UiO-66 for the Codelivery of DOX/pCRISPR, ACS Appl. Mater. Interfaces 13 (2021) 10796–10811.

[39] C.I. Ezugwu, M.A. Asraf, X. Li, S. Liu, C.-M. Kao, S. Zhuiykov, F. Verpoort, Cationic nickel metal-organic frameworks for adsorption of negatively charged dye molecules, Data Brief 18 (2018) 1952–1961.

[40] H. Vardhan, A. Mehta, C.I. Ezugwu, F. Verpoort, Self-assembled arene ruthenium metalla-assemblies, Polyhedron 112 (2016) 104–108.

[41] B. Mousavi, S. Chaemchuen, C.I. Ezugwu, Y. Yuan, F. Verpoort, The effect of synthesis procedure on the catalytic performance of isostructural ZIF-8, Appl. Organomet. Chem. 32 (2018) e4062.

[42] N. Gholampour, C.I. Ezugwu, S. Rahmdele, A.G. Gilanie, F. Verpoort, Adsorptive removal and catalytic performance of metal-organic frameworks containing mixed azolium-bipyridine ligand, Resources, Chem. Mater. 1 (2022) 201–210, https://doi.org/10.1016/j.recm.2022.07.003.

[43] N. Liu, L. Shi, X. Meng, Tuning the adsorption properties of UiO-66 via acetic acid modulation, J. Chem. Sci. 131 (2019) 1–7.

[44] F. Chioma, C.I. Ezugwu, O. Okpareke, Synthesis, characterization, DFT and biological studies of Fe(II), Cu(II), and Zn(II) complexes of keto-imine chelators, Inorganica Chim. Acta 545 (2022) 121255.

[45] P. Karthik, A.M. Shaheer, A. Vinu, B. Neppolian, Amine Functionalized Metal-Organic Framework Coordinated with Transition Metal Ions: d–d Transition Enhanced Optical Absorption and Role of Transition Metal Sites on Solar Light Driven H₂ Production, Small 16 (2020) 1902990.

[46] X. Zheng, R. Fan, Y. Song, A. Wang, K. Xing, X. Du, P. Wang, Y. Yang, A highly sensitive turn-on ratiometric luminescence probe based on postsynthetic modification of Tb³⁺@Cu-MOF for H₂S detection, J. Mater. Chem. 5 (2017) 9943–9951.

[47] A.S. Morshedy, H.M. Abd El Salam, A.M. El Naggar, T. Zaki, Hydrogen Production and In Situ Storage through Process of Water Splitting Using Mono/Binary Metal-Organic Framework (MOF) Structures as New Chief Photocatalysts, Energy Fuels 34 (2020) 11660–11669.

[48] F. Wen, X. Wang, L. Huang, G. Ma, J. Yang, C. Li, A hybrid photocatalytic system comprising ZnS as light harvester and an [Fe₂S₂] hydrogenase mimic as hydrogen evolution catalyst, ChemSusChem 5 (2012) 849–853.

[49] M. Pamei, A. Puzari, Luminescent transition metal–organic frameworks: An emerging sensor for detecting biologically essential metal ions, Nano-Struct. Nano-Objects 19 (2019) 100364.

[50] D. Sun, Y. Fu, W. Liu, L. Ye, D. Wang, L. Yang, X. Fu, Z. Li, Studies on Photocatalytic CO₂ Reduction over NH₂-UiO-66(Zr) and Its Derivatives: Towards a Better Understanding of Photocatalysis on Metal-Organic Frameworks, Chem. Eur. J. 19 (2013) 14279–14285.

[51] S. Ghosh, H. Remita, R.N. Basu, Significantly enhanced photocatalytic reduction of Cr (VI) on ZnO-conducting polymeric nanofibers heterojunction under visible-light irradiation, Appl. Catal. B: Environ. 239 (2018) 362–372.

[52] P. Xu, T.J. Milstein, T.E. Mallouk, Flat-band potentials of molecularly thin metal oxide nanosheets, ACS Appl. Mater. Interfaces 8 (2016) 11539–11547.

[53] M. Taddei, G.M. Schukraft, M.E. Warwick, D. Tiana, M.J. McPherson, D.R. Jones, C. Petit, Band gap modulation in zirconium-based metal–organic frameworks by defect engineering, J. Mater. Chem. A 7 (2019) 23781–23786.

[54] H.-Q. Xu, J. Hu, D. Wang, Z. Li, Q. Zhang, Y. Luo, S.-H. Yu, H.-L. Jiang, Visible-light photoreduction of CO2 in a metal–organic framework: boosting electron–hole separation via electron trap states, J. Am. Chem. Soc. 137 (2015) 13440–13443.

[55] D. Chen, H. Xing, C. Wang, Z. Su, Highly efficient visible-light-driven CO₂ reduction to formate by a new anthracene-based zirconium MOF via dual catalytic routes, J. Mater. Chem. 4 (2016) 2657–2662.

[56] W. Lin, H. Frei, Photochemical CO₂ splitting by metal-to-metal charge-transfer excitation in mesoporous ZrCu(I)-MCM-41 silicate sieve, J. Am. Chem. Soc. 127 (2005) 1610–1611.

[57] R. Nakamura, A. Okamoto, H. Osawa, H. Irie, K. Hashimoto, Design of all-inorganic molecular-based photocatalysts sensitive to visible light: Ti (IV)− O− Ce (III) bimetallic assemblies on mesoporous silica, J. Am. Chem. Soc. 129 (2007) 9596–9597.

[58] W. Lin, H. Frei, Anchored metal-to-metal charge-transfer chromophores in a mesoporous silicate sieve for visible-light activation of titanium centers, J. Phys. Chem. B 109 (2005) 4929–4935.